Two-Dimensional Simulations of Valveless Pumping Using the Immersed Boundary Method II

Eunok Jung* Charles S. Peskin†

December 26, 2001

Abstract

This paper extends our previous work on the two-dimensional simulations of valveless pumping using the Immersed Boundary Method. The main results of the previous work were as follows: First, despite the absence of valves, a net flow around the loop that consists of (almost) rigid and flexible parts was produced by the periodic driving force on the end of the flexible boundary. Second, the direction and magnitude of flow around the loop of tubing were determined not only by the position of the periodic forcing but also by the frequency and amplitude of the driving force. In this paper, a new driving forcing function is introduced in order to provide the more effective model of valveless pumping. We demonstrate how important the driving forcing function affects a net flow in the valveless circulatory system and investigate which parameter set of the system gives a more efficient net flow around the loop.

1 Introduction

The numerical simulations of a net flow which is generated by a valveless mechanism in a circulatory system are presented. This work was originally motivated by an biomedical objective; explain the complicated valveless blood flow mechanism in the circulation. Liebau demonstrated the various experiments of valveless pumping [26, 25, 24, 23] and observed a net flow from those experiments. His interest was motivated by the observation that sufficient blood circulation is retained in patients with probably inoperative aortic valves [42] and by the

*Oak Ridge National Laboratory, P.O. Box 2008, Bldg. 6012, MS-6367, Oak Ridge, TN 37831-6367 (junge@ornl.gov). This author's research has been authored by a contractor of the U.S. Government under Contract No. DE-AC05-00OR22725. Accordingly, the U.S. Government retains a non-exclusive, royalty-free license to publish or reproduce the published form of this contribution, or allow others to do so, for U.S. Government purposes.

†Courant Institute of Mathematical Sciences, New York University, 251 Mercer Street, New York, NY 10012 (peskin@cims.nyu.edu).

theory (William Harvey's concept of the circulation) that the heart alone is not good enough to obtain the necessary pumping, but it is assisted [17]. In our previous work, we examined flows driven by valveless pumping in Liebau's model, a closed circuit tube that consists of (almost) rigid and flexible parts. The main results of these simulations of valveless pumping were following. We observed the existence of a net flow when the periodic driving oscillation is applied on the end of flexible segments of the loop of tubing, as in the physical experiments of valveless pumping [20, 25, 31]. More startling result was that the direction and magnitude of the flow around the loop were decided not only by the position of the driving force but also by the frequency and amplitude of the driving force. Another interesting phenomenon was that a clockwise net flow seems to be associated with a standing wave along the flexible segments of tubing, whereas a counterclockwise net flow seems to be associated with a traveling wave via a peristaltic mechanism.

It has been surprisingly investigated how various applications of valveless pumping might be found in the biomedical engineering, biology, and engineering fields. For instance, early stages of the human embryonic circulation [30]; the thoracic pump theory in the blood flow mechanism during the cardiopulmonary resuscitation (CPR) (It has been reported that the heart acts as a passive conduit and the mitral valve remains open during the entire cycle of CPR [2, 6, 16, 43]); Amphioxus [41]; lymph drainage in the eye [15]; inoperative aortic valve [42]; and microelectromechanical system (MEMS) [29]. A detailed description of these applications of valveless pumping is presented in [19, 31].

Since our goal of these simulations is to make a more efficient model that is the main goal of the real world applications such as CPR or MEMS devices, it is of obvious important to know which parameter set or what kind of driving forcing function will produce a more effective net circulatory flow.

In this paper, a new driving forcing function is considered. A parameter compression duration d, that is defined by the ratio of the compression and relaxation time during a period, is introduced in this driving forcing function. The new forcing function consists of the periodic motions of compression and relaxation, whereas the old forcing function consists of the periodic motions of compression and extension on the end of the flexible segments of the loop.

We have observed that more net flow around the loop is obtained when the compression duration is close to $d = 0.5$, i.e. when the relaxation period is introduced rather than the continuous motions of the compression and expansion without the relaxation in our previous model [19]. Various parameter sets have been studied with this new driving forcing function, in order to investigate the most effective model of valveless pumping.

This paper is organized as follows; Section 2 describes the computational model of valveless pumping. A brief outline of the numerical method, immersed boundary method, and a new driving forcing function will be presented in this section. The numerical results will be discussed in section 3. In this section, the time-averaged fluxes generated by the old and new driving forcing functions will be compared. Various parameter sets will be studied with this new driving force and some spectial case studies will be also presented. Section 4 includes some conclusions and future work.

2 Computational model of the valveless pumping

2.1 The immersed boundary method

In this section, a summary of immersed boundary method that is used in our simulations of valveless pumping is described. The immersed boundary method is both a mathematical formulation and a computational method for any problem in which an incompressible viscous fluid interacts with an immersed elastic material. The idealized elastic material is treated as a part of fluid and has neither mass nor volume. The immersed elastic material moves at the local fluid velocity, while the motion of fluid is effected by this elastic material. The strength of the immersed boundary method is that the motion of the elastic material that has a complicated and time-dependent geometry is solved in a Cartesian box of fluid, instead of using a grid on the physical boundary that would be very difficult in computation. This methodology has been applied to the heart and its valves [27, 32, 33, 34, 35, 36], platelet aggregation during blood clotting [13], flow of suspensions [14], fluid dynamics of the inner ear [3], aquatic animal locomotion [9, 11], flow in collapsible tubes [40], the collapse of thin-walled veins, biofilm processes [7, 8], viscoelastic networks and cell deformation in the context [4], arteriolar flow and mass transport [1], and valveless pumping [18, 19].

The numerical algorithm of immersed boundary method has been also improved over time: improved volume conservation [38], truncated newton methods for the complex immersed elastic structure [11], immersed interface method [22], shared-memory parallel vector implementation [28], an adaptive version of Immersed Boundary Method [39], blob projection method [5], and formal second-order accuracy and reduced numerical viscosity [21].

The following is a general summary of this method. The motion of a viscous incompressible fluid is represented by Eulerian velocities and pressures on a fixed Cartesian coordinate system and the motion of the elastic materials is expressed in Lagrangian form. A typical time step of the computational method proceeds as follows: At the beginning of the time step, the fluid velocity at each point of the fluid grid and the boundary configuration of the elastic materials are known. The boundary forces are computed from the given boundary configuration, and then used to spread these boundary forces into the nearby fluid grid to evaluate the fluid forces using the Dirac delta function. With the fluid forces known, the Navier-Stokes equations are solved in order to get an updated velocity on the fluid grid. Finally, upon interpolating the updated velocity field to the boundary locations using the same delta function, the boundary is moved at the interpolated velocity. This completes the time step.

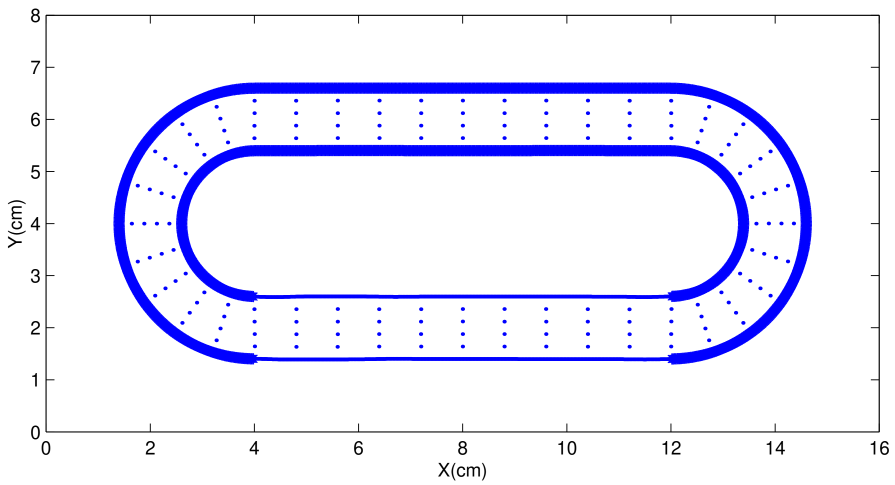

Figure 1: Initial position of two-dimensional valveless pumping: flexible boundary (thin lines), almost rigid (thick lines), and fluid markers (dots). The incompressible viscous fluid fills the entire computational box, containing the racetrack shape of the elastic material.

2.2 Computational model of valveless pumping

We shall now consider a two-dimensional computational model of valveless pumping. The racetrack shape of the elastic material, S_b for $b = 1$ (inner immersed boundary) or $b = 2$ (outer immersed boundary), is modeled as an immersed boundary in the rectangular computational domain, Ω, that is filled with incompressible fluid. Figure 1 displays the initial configuration of the two-dimensional valveless pumping. The motion of a coupled system of the fluid-immersed boundary is governed by the fluid equations in the Eulerian form, the immersed boundary equations in the Lagrangian form, and the interaction equations in the mixed Eulerian and Lagrangian forms. The equations of motions are then as follows:

The Navier-Stocks equations (fluid equations) are given by

$$\rho\left(\frac{\partial \boldsymbol{u}(\boldsymbol{x},t)}{\partial t} + (\boldsymbol{u}(\boldsymbol{x},t)\cdot\nabla)\boldsymbol{u}(\boldsymbol{x},t)\right) + \nabla p(\boldsymbol{x},t) = \mu\nabla^2\boldsymbol{u}(\boldsymbol{x},t) + \boldsymbol{F}(\boldsymbol{x},t), \quad (1)$$

$$\nabla\cdot\boldsymbol{u}(\boldsymbol{x},t) = 0, \quad (2)$$

where the constant parameters ρ and μ are the fluid density and viscosity, respectively. The fluid velocity $\boldsymbol{u}(\boldsymbol{x}, t)$, fluid pressure $p(\boldsymbol{x}, t)$, and external force density $\boldsymbol{F}(\boldsymbol{x}, t)$ are functions of a fixed Cartesian coordinates $\boldsymbol{x} = (x, y)$ and the time t.

The interaction equations between the fluid and the immersed boundary are given by

$$\boldsymbol{F}(\boldsymbol{x}, t) = \int_{S_b} \boldsymbol{f}_b(s, t)\, \delta^2(\boldsymbol{x} - \boldsymbol{X}_b(s, t))\, ds, \tag{3}$$

$$\boldsymbol{U}_b(s, t) = \int_{\Omega} \boldsymbol{u}(\boldsymbol{x}, t)\, \delta^2(\boldsymbol{x} - \boldsymbol{X}_b(s, t))\, d\boldsymbol{x}, \tag{4}$$

The configurations of the immersed boundaries at time t are $\boldsymbol{X}_b(s, t)$ parameterized by s, where $b = 1$ (inner immersed boundary) or 2 (outer immersed boundary), and $0 \leq s \leq L_1$ for the inner immersed boundary and $0 \leq s \leq L_2$ for the outer immersed boundary. L_1 and L_2 are the unstressed lengths of the inner and outer boundaries, respectively. $\boldsymbol{f}_b(s, t)$ are the boundary force densities and $\boldsymbol{U}_b(s, t)$ are the boundary velocities, for $b = 1$ (inner immersed boundary) or 2 (outer immersed boundary). The delta function is a product of two one-dimensional delta functions: $\delta^2(\boldsymbol{x}) = \delta(x)\delta(y)$.

The immersed boundary equations are given by

$$\frac{\partial \boldsymbol{X}_b(s, t)}{\partial t}(s, t) = \boldsymbol{U}_b(s, t), \tag{5}$$

$$\boldsymbol{f}_b(s, t) = -(\kappa_t)_b(\boldsymbol{X}_b(s, t) - \boldsymbol{Z}_b(s, t)) + \kappa_c \left(\frac{\partial^2 \boldsymbol{X}_b(s, t)}{\partial s^2} \right), \tag{6}$$

where κ_t is a stiffness constant between the physical boundary and the target positions and κ_c is a stiffness constant of a linear spring between two adjacent boundary points. In the boundary force density equation (6), the given function $\boldsymbol{Z}_b(s, t)$ is called the target position of the immersed boundary. This target position is the source of applying periodic forcing to the immersed boundaries. The derivation of the boundary force will be given in the following subsection. Note that the choice of the target position is a main difference from the previous work [].

Since we used the same numerical method as the previous work, we present only a brief summary of numerical method in this paper. The rectangular computational box is discretized by a Cartesian grid at time $t = n\Delta t$: $\boldsymbol{x}^n_{jk} = \boldsymbol{x}(j\Delta x, k\Delta y, n\Delta t)$, where $j = 0, \ldots, N_x - 1$, $k = 0, \ldots, N_y - 1$, and $n = 0, 1, \ldots$. The immersed boundary are represented by a collection of moving points at time $t = n\Delta t$: $\boldsymbol{X}^n_{bl} = \boldsymbol{X}_b(l\Delta s_b, n\Delta t)$, where $l = 1, \ldots, M_1$ and $L_1 = M_1\Delta s_1$ for $b = 1$ (inner immersed boundary) or $l = 1, \ldots, M_2$ and $L_2 = M_2\Delta s_2$ for $b = 2$ (outer immersed boundary). Since the boundaries are closed, $\boldsymbol{X}_1(M_1 + 1) = \boldsymbol{X}_1(1)$ or $\boldsymbol{X}_2(M_2 + 1) = \boldsymbol{X}_2(1)$.

The updated $\boldsymbol{u}^{n+1}$, $\boldsymbol{X}^{n+1}_b$ from given $\boldsymbol{u}^n$, $\boldsymbol{X}^n_b$ are computed as follows:

Step 1. Compute the immersed boundary force density $\boldsymbol{f}_b^n$ from the given boundary configuration $\boldsymbol{X}_b^n$ and the target positions $\boldsymbol{Z}_b^n$. For $l = 1, \ldots, M_b$, and $b = 1$ (inner boundary) or 2 (outer boundary),

$$\boldsymbol{f}_{bl}^n = -(\kappa_t)_l(\boldsymbol{X}_{bl}^n - \boldsymbol{Z}_{bl}^n) + \kappa_c \left(\frac{\boldsymbol{X}_{b(l+1)}^n - 2\boldsymbol{X}_{bl}^n + \boldsymbol{X}_{b(l-1)}^n}{\Delta s_b^2} \right), \tag{7}$$

where Δs_b is an arc length.

Step 2. Spread this boundary force density $\boldsymbol{f}_b^n$ into the nearby 16 lattice points in order get the fluid force density $\boldsymbol{F}^n$.

$$\boldsymbol{F}_{jk}^n = \sum_{b=1}^{2} \sum_{l=1}^{M_b} \boldsymbol{f}_{bl}^n \delta_h^2(\boldsymbol{x}_{jk} - \boldsymbol{X}_{bl}^n)\Delta s_b \qquad \text{for} \quad j,k = 0,1,\ldots,N-1, \tag{8}$$

where δ_h^2 is a smoothed approximation to the two-dimensional 4 points Dirac delta function.

Step 3. Solve the Navier-Stokes equations for the updated fluid velocity $\boldsymbol{u}^{n+1}$ and p^{n+1} from $\boldsymbol{u}^n$ and $\boldsymbol{F}^n$ in the Step 2.

$$\rho \left(\frac{\boldsymbol{u}^{n+1} - \boldsymbol{u}^n}{\Delta t} + \boldsymbol{u}^n \cdot \nabla_h^{\pm} \boldsymbol{u}^n \right) + \boldsymbol{D}^0 p^{n+1} = \mu \Delta_h \boldsymbol{u}^{n+1} + \boldsymbol{F}^n, \tag{9}$$

$$\boldsymbol{D}^0 \cdot \boldsymbol{u}^{n+1} = 0. \tag{10}$$

The implicit first order difference operators are used in time and space. The backward Euler scheme for the Stokes system, the upwind scheme for the convection term, the centered difference operator for the pressure, and the standard 5 points Laplacian operator for the viscous term are chosen. The periodic boundary conditions are imposed on the computational domain. Because of choice of boundary condition, the fast fourier transform (FFT) and inverse FFT algorithms are used to solve (9) and (10).

Step 4. Interpolate this updated fluid velocity $\boldsymbol{u}^{n+1}$ and apply no-slip condition to get the updated immersed boundary velocity $\boldsymbol{U}_b^{n+1}$ and position $\boldsymbol{X}_b^{n+1}$.

$$\boldsymbol{U}_{bl}^{n+1} = \sum_{j,k=0}^{N-1} \boldsymbol{u}_{jk}^{n+1} \delta_h^2(\boldsymbol{x}_{jk} - \boldsymbol{X}_{bl}^n) h^2, \tag{11}$$

$$\boldsymbol{X}_{bl}^{n+1} = \boldsymbol{X}_{bl}^n + \Delta t \boldsymbol{U}_{bl}^{n+1}. \tag{12}$$

This completes the description of the process (Steps 1–4, above) by which the quantities $\boldsymbol{u}$ and $\boldsymbol{X}$ are updated.

2.3 Boundary force determination

The force density imposed on the immersed boundary consists of the two terms: the target position term, $\boldsymbol{f}_{bt}$, and the curvature-like term, $\boldsymbol{f}_{bc}$ for $b = 1$ (inner boundary) or $b = 2$ (outer boundary).

In the first term, $\boldsymbol{f}_{bt}$, of the equation (6), the given target position $\boldsymbol{Z}_b(s,t)$ actually drive a complex dynamic system of flow around the loop of tubing. The stiffness constant, κ_t, represents the property of elasticity for the two different compliances of the tubing. The very large number is chosen for the almost rigid part of tubing; $\kappa_t = 26000$, and much smaller number is chosen for the flexible part; $\kappa_t = 900$. Both inner and outer boundaries have the same values of κ_t. The target position $\boldsymbol{Z}_b(s,t)$ consists of the time-independent and time-dependent parts. The main purpose of this time-independent target position is to keep the racetrack shape of the flow loop during the simulated time. The time-independent target function is applied on the whole loop of tubing except the part that the driving force is imposed. The left $1/3$ of the flexible segment is chosen for applying the periodic force in most of our simulations. The physical position with the thick curves of the loop in Figure 1, almost rigid part, keeps the racetrack shape as given in the initial configuration. This is because of choice of the large number for the stiffness constant κ_t. We now present the time-dependent target position. The role of the time-dependent target position is to impose the periodic force in some portion of the flexible segment in order to get a flow around the loop of tubing. A parameter compression duration, d, is introduced in this new periodic forcing function. The compression duration is defined by the ratio of the time for compression and relaxation during a period, T. For instance, if $d = 0.5$, then the compression is applied for the first half of the periodic time and the relaxation for the rest half of the period. Note that, in the previous work, the flows were all driven by the continuous motions of compression and expansion on one end of the flexible segment of the loop. This change in the forcing function is the main difference between the previous and present studies. It is surprising to see how small change in the forcing function makes more effective model of valveless pumping.

We describe the mathematical formulations of the time-dependent target position in one end of the flexible segment of the loop of tubing.

Let $\boldsymbol{Z}_b(s,t) = (Z_{xb}(s), Z_{yb}(s,t))$, where s is restricted to the range of values that defines the portion of the flexible segment that is imposed the periodic forcing. Let the target position on the flexible segment begins at $x = x_0$ and ends at $x = x_1$.

Define

$$A(s,t) = A_0 \sin\left(\frac{2\pi t}{dT}\right) \sin\left(\pi \frac{Z_{xb}(s) - x_0}{x_1 - x_0}\right),$$

where A_0 is the amplitude of the target position motion, T is its period, and d is compression duration. If $d = 0.5$ is chosen, the the function $A(s,t)$ is the half sine function with the wavelength $2(x_1 - x_0)$ at the fixed time.

$\boldsymbol{Z}_b(s,t)$ is defined as follows:

$$Z_{bx}(s,t) = X_b(s,0), \qquad \text{for } b = 1 \text{ or } b = 2.$$

For $0 < \text{mod(t, T)} \le \text{dT}$,

$$Z_{by}(s,t) = \begin{cases} 0.25Y_{scale} + 0.5l + A(s,t) & \text{if } b = 1 \text{ (inner boundary)}, \\ 0.25Y_{scale} - 0.5l - A(s,t) & \text{if } b = 2 \text{ (outer boundary)}, \end{cases}$$

and for $\text{dT} < \text{mod(t, T)} \le \text{T}$,

$$Z_{by}(s,t) = X_b(s,0), \qquad \text{for } b = 1 \text{ or } b = 2.$$

where l is the resting diameter of the tube and Y_{scale} is the width of the computational domain.

In Figure 2, the y component of the target positions at the center of the top flexible segment that the driving force is applied are plotted as a function of the time. The x component of the target positions is fixed as $\frac{x_0+x_1}{2}$ at the top flexible segment. The old time-dependent target position (in the previous paper) and the new time-dependent target position (in the present paper) is plotted in the top frame and bottom frame, respectively. Parameters $T = 1$ s, $A_0 = 0.6$ cm, and $d = 0.5$ is chosen.

The negative, zero, and positive values represents the motion of the compression, relaxation, and expansion of the portion on the flexible segment that the time-dependent target function is applied. Flows are driven by the periodic motions of the compression and relaxation in the time-dependent target position are used in the present study, whereas the continuous motions of compression and expansion in the time-dependent target position were used in the previous work.

In the second term, $\boldsymbol{f}_{bc}$, of the equation (6), the curvature-like term models elastic property of the immersed boundary. This force is driven from a time dependent nonnegative energy function $E_b(\boldsymbol{X}_1, \boldsymbol{X}_2, \ldots, \boldsymbol{X}_{Mb}, t)$ for $b = 1$ (inner boundary) or $b = 2$ (outer boundary). Energy function achieves the minimum at the desired configuration. We assume that the resting length between successive points on the immersed boundary is zero. An energy function which has the desired properties for our model is as follows:

For $b = 1$ (inner boundary) or $b = 2$ (outer boundary),

$$\begin{aligned} E_b(\boldsymbol{X}_1, \boldsymbol{X}_2, \ldots, \boldsymbol{X}_{M_b}, t) &= \frac{1}{2}\kappa_c \sum_{l=1}^{M_b} \|\boldsymbol{X}_{l+1} - \boldsymbol{X}_l\|^2 \\ &= \frac{1}{2}\kappa_c \sum_{l=1}^{M_b} \left((x_{l+1} - x_l)^2 + (y_{l+1} - y_l)^2 \right), \end{aligned}$$

and the forces at each boundary points are

$$\begin{aligned} \boldsymbol{f}_b^*(\boldsymbol{X}_l) &= -\frac{\partial E_b}{\partial \boldsymbol{X}_l}, \qquad \text{for} \quad l = 1, \ldots, M_b \\ &= \kappa_c \left(\frac{x_{l+1} - 2x_l + x_{l-1}}{\Delta s_b}, \frac{y_{l+1} - 2y_l + y_{l-1}}{\Delta s_b} \right), \\ &= \kappa_c \left(\frac{\boldsymbol{X}_{l+1} - 2\boldsymbol{X}_l + \boldsymbol{X}_{l-1}}{\Delta s_b} \right), \end{aligned}$$

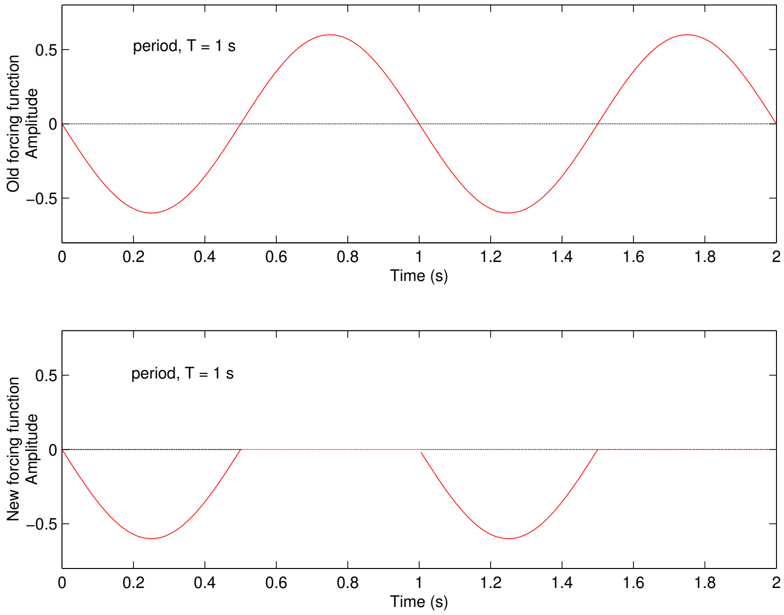

Figure 2: The y component of the target positions at the center of the top flexible segment that the driving force is applied are plotted as a function of the time. In the old time-dependent target position at the top frame, the continuous motions of contraction and expansion are chosen for the driving force. In the new time-dependent target position at the bottom frame, the periodic motions of the compression and relaxation are chosen for the driving force. Parameters $T = 1\ s$, $A_0 = 0.6\ cm$, and $d = 0.5$ are chosen.

where $\boldsymbol{X}_l = (x_l, y_l)$ for $l = 1, \ldots, M_b$. Therefore, the boundary force density is derived as one in equation (6).

2.4 Parameters

The CGS units are used in this work. We characterize the motions of flows with the dimensionless number, Reynolds number Re. The Reynolds number is defined by $Re = \frac{\rho U l}{\mu}$, where l is a diameter of the tube, ρ is a constant density, μ is viscosity, and U is a time-averaged velocity. Note that since the flow is incompressible and the simulated time in our computations is chosen until the flow become a steady state, any choice of cross sections of the loop should give the same time-averaged velocity. The range of the Reynolds number in this paper is between 0 to around 193. Any nonzero Reynolds number implies an existence of a net flow with the either clockwise or counterclockwise direction around the loop in the valveless pumping mechanism.

The physical and numerical parameters are presented in Tables 1 and 2. In

Table 1: Physical parameters.

Physical parameters	Symbol	
density	ρ	1 g/cm^3
viscosity	μ	0.01 g/cm $\cdot s$
circumference of a loop	D	28.57 cm
diameter of tube	l	0.6 cm
computational domain	$X_{scale} \times Y_{scale}$	16 cm $\times$ 8 cm
length of the flexible segment	$l_{flexible}$	8 cm
period	T	0.05 s $\sim$ 4 s
amplitude(target)	A_0	0.4 cm and 0.6 cm
compression duration	d	0 $\sim$ 1
fraction compressed		0 $\sim$ 0.5 $l_{flexible}$ cm
duration of experiment	t_{max}	100 s
stiffness constant(almost rigid)	κ_t	26000 g/s$^2\cdot$ cm
stiffness constant(flexible)	κ_t	900 g/s$^2\cdot$ cm
stiffness constant(curvature)	κ_c	120 $g\cdot$ cm/s^2

Table 2: Computational parameters.

Computational parameters	Symbol	
fluid lattice	$N_x \times N_y$	256 $\times$ 128
number of immersed boundary points	$M_1 + M_2$	3654 or 7308
meshwidth	$h = \Delta x = \Delta y$	0.0625 cm
initial distance between boundary points	$\Delta s_1 = \Delta s_2$	$h/4 = 0.0156$ cm or $h/8$ $= 0.0078$ cm
time step duration	Δt	0.5 h^2 = 0.00195 s

this paper, the four parameters, amplitude of the target positions, frequency and compression duration of the driving force, and fraction of the flexible segment being compressed, are varied and other physical parameters are fixed. For some cases of our simulations, it has been observed that the motions of the flexible boundaries are too active to get leaking fluid markers though the flexible boundaries. The volume (or area) could be conserved for those cases as the initial distance between boundary points is chosen by $h/8$, which implies that the twice more immersed boundary points than other general cases are considered. We investigate how these parameters effect the flow dynamics of valveless pumping. In particular, the direction and magnitude of a net flow around the loop are the main focus of this research.

3 Results and discussion

Our main objective is to make a more efficient model of valveless pumping. In this paper, flows are induced by a new driving force governing by the periodic motions of compression and relaxation on the end of the flexible segments. We will show that this new driving force generate more efficient model of valveless pumping than the previous one in [19]. With this new driving force, we have also observed the same phenomena we presented in the previous work;

- Existence of a net flow around the loop despite of the lack of valves.
- Direction and magnitude of flow are determined by the parameters such as frequency, amplitude, compression duration of the driving force and the fraction of the flexible boundary being compressed.
- Wave motions along the flexible segments are governed by a standing wave pattern for the clockwise net flows and the almost zero net flows and a traveling wave pattern for the counterclockwise net flows.

Throughout this paper, the fraction of the flexible boundary being compressed is called the fraction compressed.

The first two phenomena will be discussed in the parameter studies and the third phenomenon will be presented in the case studies. The complex fluid dynamics of valveless pumping is governed not only by the driving force but also by the physical parameters of the loop of tubing, such as stiffness constants that represent the elasticity of the two different compliances, diameter of the tube, circumference of the loop, and the ratio of the length of the (almost) rigid and flexible boundaries. Our research in this paper is focused on only the parameter studies from the driving force, since the driving force is the critical factor to produce a net flow around the loop. Four parameters, frequency, amplitude, compression duration of the driving force and fraction compressed, are chosen.

In this section, we will first compare the computational models generated by the old and new forcing functions by the time-averaged fluxes as functions of the period and then investigate the fluid mechanism of valveless pumping by the parameter studies based on the four parameters we mentioned above. These parameter studies provide us how carefully we choose a set of parameters in order to get an efficient flow. In the last subsection, we will observed some qualitative characters in the motions of flows from the most interesting three cases; maximum clockwise flow, almost zero flow, and counterclockwise flow.

3.1 Comparison of the computational models generated by the old and new forcing functions by the time-averaged fluxes as functions of the period.

In this subsection, we compare the flows generated by the old and new forcing functions.

Figure 3 displays the time-averaged fluxes as functions of the period of the driving oscillation. Flows induced by the old and new forcing functions are represented by the circles and stars, respectively. Each pair of data points summarizes a separate numerical experiment during the simulated time 100 s. Positive flux denotes a clockwise net flow of the loop of tubing and negative flux denotes a counterclockwise net flow. The periodic oscillation is applied on

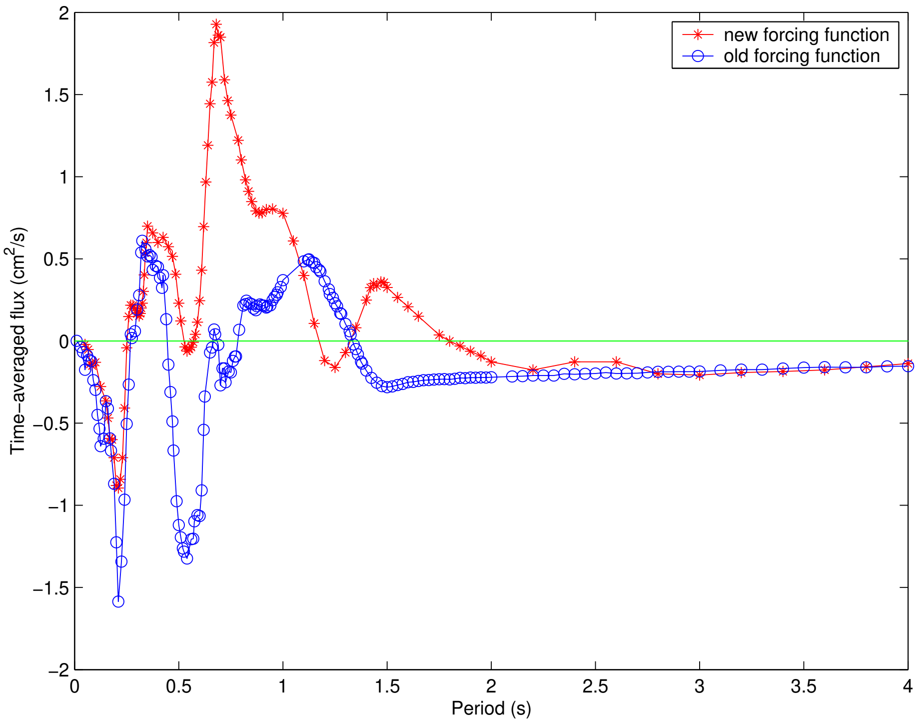

Figure 3: The time-averaged flux as a function of the period of the driving oscillatory are plotted for the flows driven by the old (circles) and new (stars) forcing functions. Each pair of data points summarizes a separate numerical experiment during the simulated time 100 s. Positive flux denotes a clockwise net flow of the loop of tubing and negative flux denotes a counterclockwise net flow. Parameters, $A_0 = 0.6\ cm$ and $d = 0.5$ are chosen.

the left 1/3 of the flexible segments of the loop and the amplitude of the target positions $A_0 = 0.6$ cm is chosen. The compression duration $d = 0.5$ is chosen for the flows driven by the new forcing function. Other parameters are presented in Tables 1 and 2. The results from Figure 3 are as follows:

- The new forcing function generates much more fluxes in the clockwise direction than the old forcing function. Note that since the driving force is applied on the left 1/3 of the flexible segments of the loop, the clockwise direction of a net flow is the same direction that has been observed in physical experiments by Liebau [], Kilner [], and other previous researchers []. The Reynolds numbers for the clockwise net flows driven by the new forcing function are in the range of 0 and 193, whereas the Reynolds numbers for the clockwise net flows driven by the old forcing function are between 0 and 70.

- The two curves are qualitatively similar curves. In both curves,
  - Each nonzero data represents an evidence of a net flow existence.
  - The direction of flow around the loop is changed several times in the range of period from 0.2 to 2.
  - The magnitude of flow around the loop is determined by the period. After the period 2.2 s, the magnitudes of flows in both curves stay very close and the time-averaged flux tends to 0.2 cm^2/s.
  - Almost zero flows at some finite periods that are not the extreme cases are observed, although the driving forces are applied on the asymmetric locations that may produce the asymmetric mechanism to the system.

3.2 Parameter studies

In this subsection, we investigate which parameter set provides more efficient model of valveless pumping. The four parameters from the driving force, frequency, amplitude, compression duration of the driving oscillation and the fraction of the flexible boundary being compressed, are chosen to vary.

This subsection consists of the following parameter studies:

- Parameter study 1: Time-averaged flux vs. Period at $A_0 = 0.6$ cm and $d = 0.5$ and 1
- Parameter study 2: Time-averaged flux vs. Compression duration at $A_0 = 0.6$ cm and $T = 0.21, 0.68, 1.35$, and 3 s
- Parameter study 3: Time-averaged flux vs. Compression duration at $T = 0.68$ s and $A_0 = 0.5$ and 0.6 cm
- Parameter study 4: Time-averaged flux vs. Amplitude at $d = 0.5$ and $T = 0.21, 0.24, 0.68$, and 1.5 s

The fraction compressed is chosen by $1/3$ for the above cases, which implies that the driving force is applied on the left $1/3$ of the flexible segments.

- Parameter study 5: Time-averaged flux vs. Fraction compressed at $A_0 = 0.6$ cm, $d = 0.5$, and $T = 0.68$ s

In these parameter studies, the time-averaged fluxes are computed on the vertical cross section through the middle of the straight segment of tubing at the top of race track and those are plotted as a function of one of the four parameters listed above for each parameter study. Other parameters are presented in Tables 1 and 2. Each data point summarizes a separate numerical experiment of 100 s simulation time. Positive flux denotes the clockwise flow around the loop and negative flux denotes the counterclockwise flow.

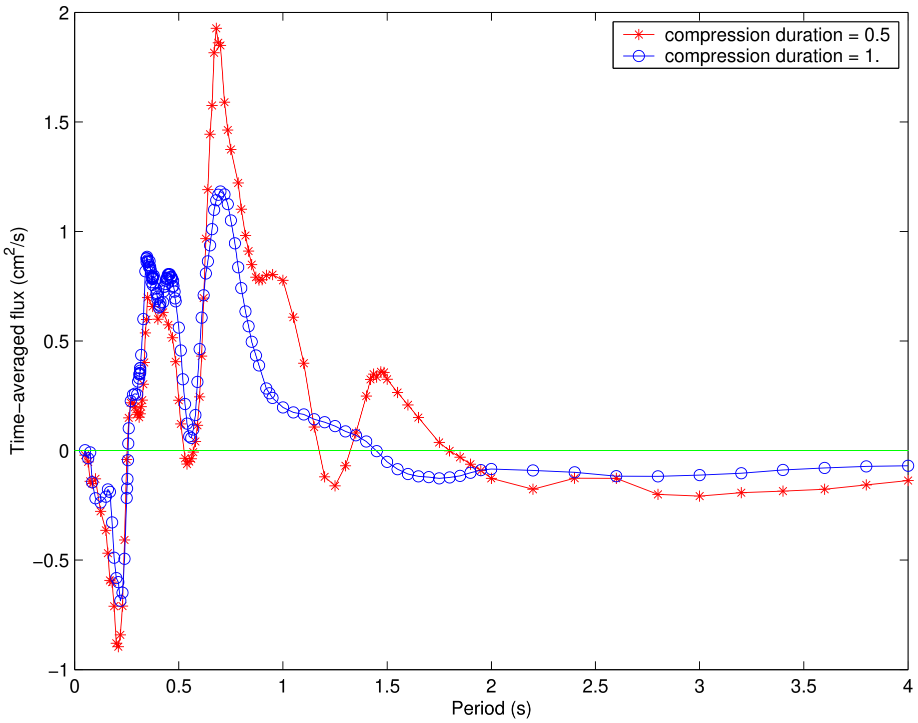

Figure 4: The time-averaged flux as a function of the period at the compression durations $d = 0.5$ (starts) and $d = 1$ (circles). The amplitude of driving oscillation $A_0 = 0.6$ cm is chosen.

Parameter study 1. Time-averaged flux vs. Period at $A_0 = 0.6$ cm and $d = 0.5$ and 1. Since the frequency has been considered as a critical parameter to determine the direction and amplitude of a net flow around the loop from the previous work [19], we start the parameter study with varying the frequency.

The choice of the compression duration $d = 1$ is a natural way to start investigation because the compression duration is a new parameter introduce in this paper and $d = 1$ implies that the driving function is generated by only the compression without relaxation. First, the time-averaged flux as a function of the period is investigated at $A_0 = 0.6$ cm, $d = 1$, and fraction compressed $= 1/3$ (see the starts in Fig. 4). The maximum flux is observed at $T = 0.68$ s. This flow has the clockwise direction and Reynolds number 193. Then, the period (1/frequency) is fixed at $T = 0.68$ s and the compression duration is varied. Like a real world problem CPR, more flux could be obtained around the compression duration $d = 0.5$ rather than $d = 1$ (see circles in Fig. 5). Now, the time-averaged fluxes are computed again as functions of the period at $d = 0.5$.

Figure 4 displays the time-averaged fluxes as function of the period at the compression durations $d = 0.5$ (starts) and $d = 1$ (circles). The amplitude of driving oscillation $A_0 = 0.6$ cm is chosen. The shape of two curves is quantitatively close. The most of experiments inthe compression duration $d = 0.5$ (stars) has more net fluxes than ones in compression duration $d = 1$ (circles). For the long period like after the period $T = 3$ s, the magnitudes of flows for $d = 1$ are reduced by around half factor of the magnitudes of flows for $d = 0.5$. Note that the magnitudes of flows generated by the new forcing function are doubled of ones by the old forcing function.

The most important result from this parameter study is that the frequency is a crucial factor to determine the direction and magnitude of a net flow around the loop.

Parameter study 2. Time-averaged flux vs. Compression duration at $A_0 = 0.6$ cm and $T = 0.21, 0.68, 1.35$, and 3 s. Figure 5 displays the time-averaged fluxes as functions of the compression duration at the four periods, $T = 0.21, 0.68, 1.35$, and 3 s. The amplitude of driving oscillation $A_0 = 0.6$ cm is chosen. From the result based on the Parameter study 1 (Figure 4), the period $T = 0.21$ s (squares) and $T = 0.68$ s (circles) has the maximum counterclockwise and clockwise net flow around the loop, respectively. Other two parameters $T = 1.35$ s (stars) and $T = 3$ s (triangles) are arbitrary chosen. The twenty equal-space compression durations from 0.1 to 1 are chosen. For all four periods, more fluxes are obtained if $d \neq 0$, which implies that the flow is driven by the periodic motions of compression and relaxation. More flux is obtained near $d = 0.5$ for the period $T = 0.68$ s and between $d = 0.5$ and $d = 0.8$ for $T = 0.21$ s. It is observed in Figure 5 that there exists at least two turning points (changing flow direction) near $d = 0.475$ and $d = 0.8$ for $T = 1.35$ s and one point near $d = 0.25$ for $T = 3$ s. The time-averaged fluxes for $T = 0.21$ s and $T = 0.68$ s are, however, all negative (counterclockwise flow) and positive (clockwise flow) for any compression durations, respectively.

Overall, the compression duration of the driving oscillation affects not only magnitude but also direction of a net flow around the loop.

Parameter study 3. Time-averaged flux vs. Compression duration at $T = 0.68$ s and $A_0 = 0.5$ and 0.6 cm. Figure 6 displays the time-averaged fluxes as functions of the compression duration at the amplitude of the driving oscillation (the prescribed time-dependent target positions) at $A_0 = 0.5$ and 0.6 cm. The period of the driving oscillation $T = 0.68$ s is chosen. More efficient fluxes are obtained around $d = 0.5$ for $A_0 = 0.6$ cm (triangles) and between $d = 0.4$ and $d = 0.6$ for $A_0 = 0.5$ cm (circles). The magnitudes of flows in $A_0 = 0.6$ cm are almost doubled as ones in $A_0 = 0.5$ cm over the compression duration range from 0.1 to 1. The amplitude of the driving oscillation also affects the magnitude of a net flow around the loop.

Parameter study 4. Time-averaged flux vs. Amplitude at $d = 0.5$ and $T = 0.21, 0.24, 0.68$, and 1.5 s. Figure 7 displays the time-averaged fluxes as functions of the amplitude of the driving oscillation at the four periods, $T = 0.21, 0.24, 0.68$, and 1.5 s.

As we observed in the previous paper, the results in Figure 7 also show that

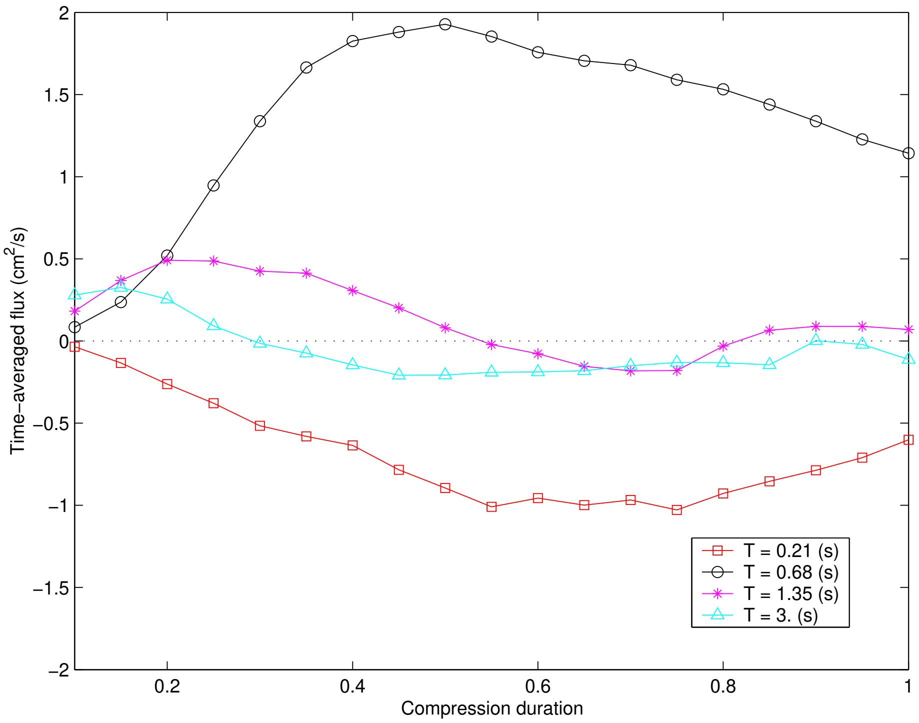

Figure 5: The time-averaged fluxes as functions of the compression duration at the four periods, $T = 0.21$ (squares), 0.68 (circles), 1.35 (stars), and 3 s (triangles). The amplitude of driving oscillation $A_0 = 0.6$ cm is chosen.

the amplitude of the driving oscillation affects the magnitude and direction of the net flow around the loop of tubing. At the low amplitude of the driving oscillation, the magnitudes of flows are small for all four periods. The direction of flow is changed at the critical amplitude for the three periods, $T = 0.24, 0.68$, and 1.5 s. For $T = 0.68$ s (circles) and 1.5 s (squares), the flow changes from the counterclockwise direction to the clockwise direction near $A_0 = 0.38$ cm and $A_0 = 0.45$ cm, respectively. The period $T = 0.68$ s has the strong clockwise net flows at high amplitude, whereas the period $T = 1.5$ s has the weak clockwise net flows. For $T = 0.21$ s (stars) and 0.24 s (pluses), the net flows have the counterclockwise direction at high amplitude, but one, $T = 0.24$ s, has the clockwise flow and the other, $T = 0.21$ s, has the counterclockwise flow at low amplitude.

From the Figures 6 and 7, it is obvious to see that the amplitude of the driving oscillation is also an important factor to determine the magnitude and direction of flow around the loop.

Parameter study 5. Time-averaged flux vs. Fraction compressed

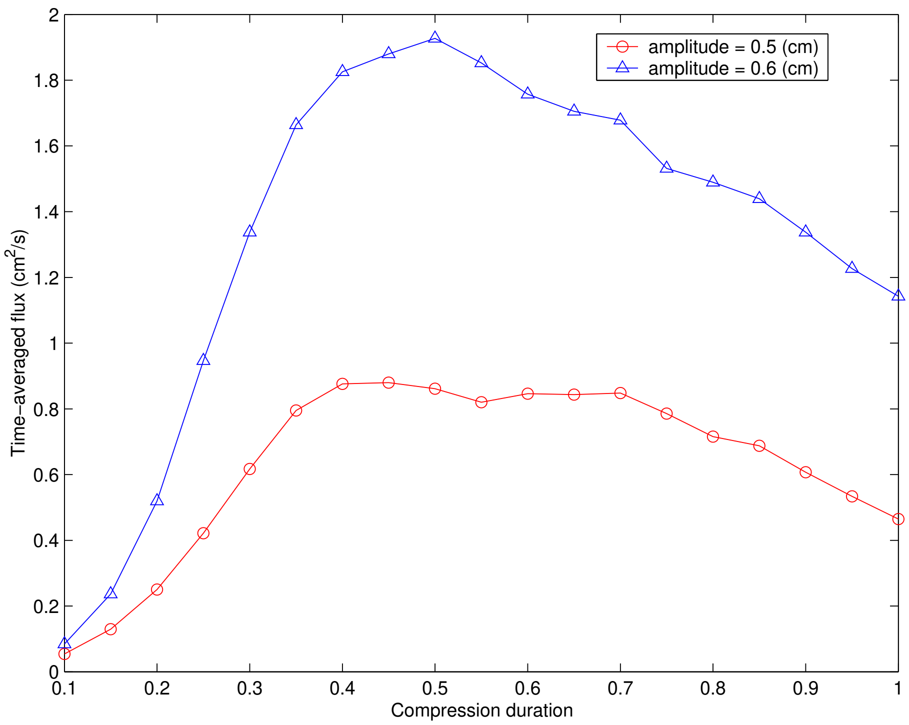

Figure 6: The time-averaged fluxes as functions of the compression duration at the amplitude of the driving oscillation $A_0 = 0.5$ and 0.6 cm. The period of the driving oscillation$T = 0.68$ s is chosen.

at A_0 = 0.6 cm, d = 0.5, and T = 0.68 s. Until now, the left 1/3 of the flexible segments of the loop is chosen to provide the periodic forcing. In this subsection, the parameter fraction compressed is varied. The twenty equal-space fractions compressed are chosen from 0 to 0.5. Recall the definition of the fraction compressed. The fraction compressed is defined by the fraction of the flexible boundary being compressed. If the fraction compressed is equal to 0.3, then it implies that the driving force is applied on the left 0.3 of the flexible segments of the flow loop.

Figure 8 displays the time-averaged fluxes as functions of the fraction compressed at $T = 0.68$ s, $d = 0.5$, and $A_0 = 0.6$ cm. As we expected, the magnitude of the flow is dependent on the fraction compressed. More interesting phenomenon is that the direction of a net flow is also changed at the critical value of the fraction compressed. In Figure 8, this critical fraction compressed is around 0.225. The curve is actually concave down and has negative (counterclockwise flows) until the fraction compressed reaches the critical value and then it is increased very fast and has positive (clockwise flows). It is obvious to

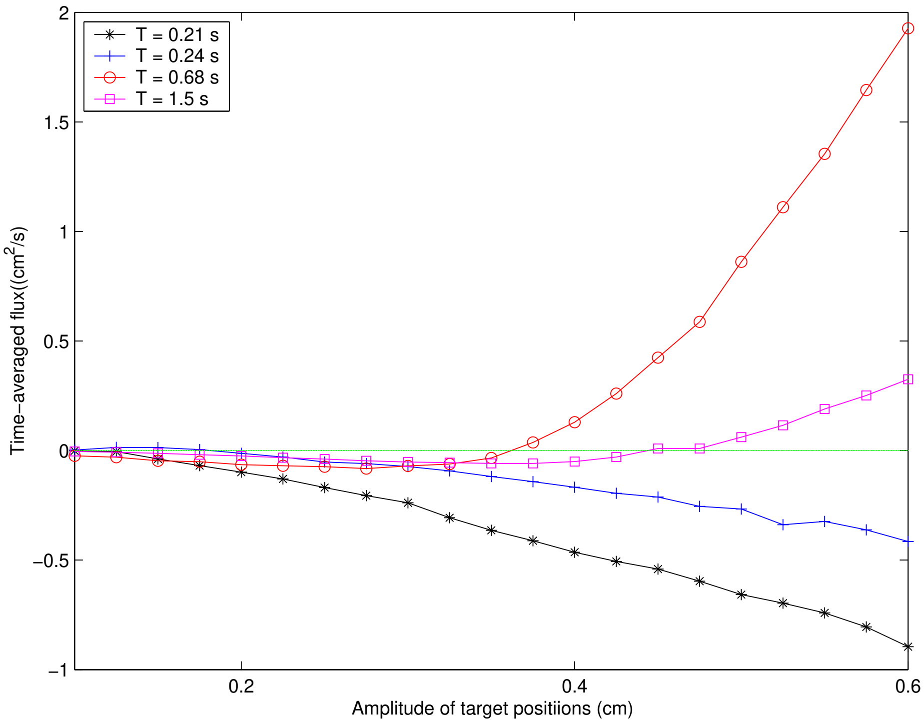

Figure 7: Tthe time-averaged fluxes as functions of the amplitude of the driving oscillation for the four periods, $T = 0.21$ (stars), 0.24 (pluses), 0.68 (circles), and 1.5 s (squares). The compression duration of the driving oscillation $d = 0.5$ is chosen.

see the nonlinearity of fluid from this curve.

3.3 Case Studies

We have investigated by the parameter studies how a set of parameters affects the motions of flow driven by valveless pumping. In parameter studies, since the time-averaged flux is used to show the existence of a net flow and to determine the amplitude and direction of a net flow around the loop, the detailed fluid dynamics of valveless pumping and how the fluid markers move around the loop could not presented. In this section, we present the three special cases of valveless pumping in order to investigate the detailed fluid mechanism of valveless pumping. The case studies are based on the results from the curve that is marked with stars in Figure 4. The amplitude $A_0 = 0.6$ cm, compression duration $d = 0.5$, simulated time $t = 100$ s, and fraction compressed $= 1/3$ are chosen. Other parameters are given in Tables 1 and 2. The maximum clockwise and countclockwise flows are obviously the first choice of case studies because

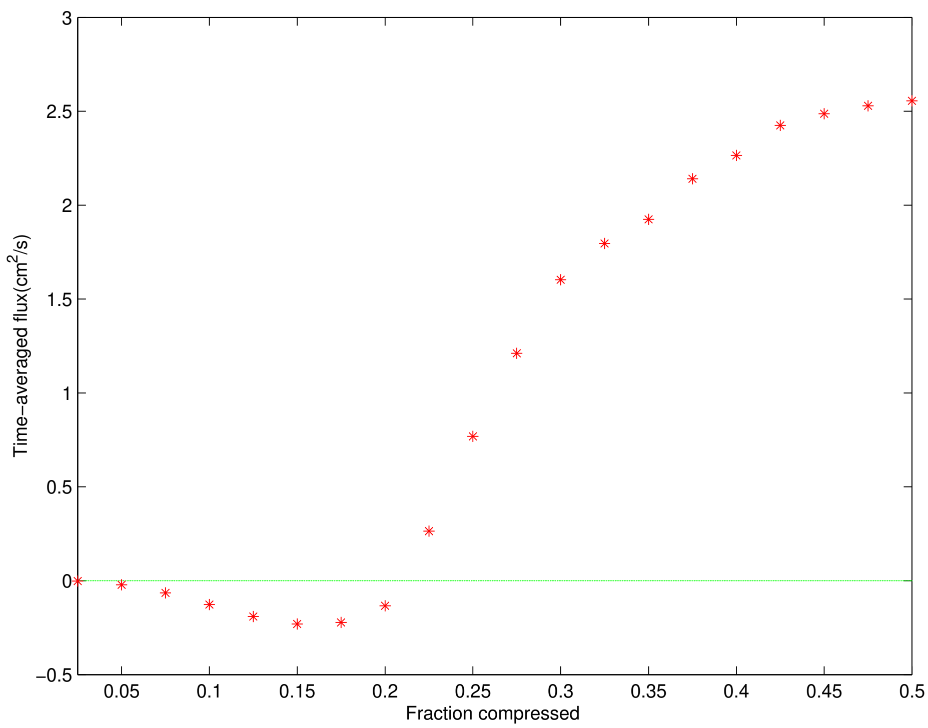

Figure 8: The time-averaged fluxes as functions of the fraction compressed at $T = 0.68$ s, $d = 0.5$, and $A_0 = 0.6$ cm.

the main goal is to produce more flux by the valveless pumping if this model is applied to the practical applications like CPR or MEMS. The third choice is a case that has an almost zero net flow around the loop. This choice is also an interesting case because the symmetric system of fluid around the loop is actually induced by the asymmetry: that is, the driving force which is applied on the asymmetric location, left 1/3 of the flexible segments may cause the asymmetry into the flow system. The periods for these three cases are $T = 0.21$ s for the maximum net counterclockwise flow, $T = 0.68$ s for the maximum net clockwise flow, and $T = 1.8$ s for the almost zero net flow. First, the detailed motion of each flow has been investigated and compared qualitatively in the following ways:

- Time-averaged fluxes as functions of the pumping cycles computed on the vertical cross section through the middle of the straight segment of the loop at the top of racetrack
- The motions of wave along the top of the flexible segments over one cycle of the periodic steady-state

- Fluid mixing

In order to show that the result does not depend on the initial conditions, these three cases are combined together during a experiment. The period $T = 0.68$ s (maximum clockwise flow) is chosen during the first 20 s, the 1/3 of the simulated time $t = 60$ s, $T = 1.8$ s (almost zero flow) during the next 20 s, and $T = 0.21$ s (maximum counterclockwise flow) is chosen during the last 20 s. All other parameters are fixed *during* the simulated time 60 s. The angles from the center of the computational domain, $(x, y) =$ (8 cm, 4 cm), to the positions of the fluid markers inside the flow loop are measured during the simulated time $t = 60$ s, in order to check the direction of a net flow.

- Flow which is induced by changing the period *during* a experiment: periods $T = 0.68$ s for the first 20 s, $T = 1.8$ s for the next 20 s, and $T = 0.21$ s for the last 20 s.

Time-averaged fluxes as functions of the pumping cycles. Figure 9 displays the time-averaged fluxes as functions of the pumping cycles during the simulated time $t = 100$ s. The case of maximum net flow in the clockwise direction, almost zero flow, and maximum net flow in the counterclockwise direction are considered from top and bottom. Each dot represents a time-averaged flux during the corresponding number of cycle from the beginning $t = 0$. Positive flux denotes the clockwise flow and negative flux denotes the counterclockwise flow. In the top frame (maximum clockwise flow at $T = 0.68$ s), the time-averaged flow around the flow loop during $t = 100$ s tends to 1.9273 cm^2/s. The total number of the pumping cycles is 147. The time-averaged flux curve is rapidly increased until around 15 cycles and the flow already stays the steady state near 50 cycles. The steady state net flow for $T = 0.68$ s has the direction in the clockwise and the Reynolds number is around 193. In the middle frame (almost zero flow at $T = 1.8$ s), the time-averaged flow around the flow loop during $t = 100$ s tends to 0. The curve stays almost constant near zero through the simulated time $t = 100$ s. The steady state net flow for $T = 1.8$ s has an almost zero net flux. In the bottom frame (maximum counterclockwise flow at $T = 0.21$ s), the curve is smoothly decreasing and the time-averaged flow around the flow loop during $t = 100$ s tends to -0.8951 cm^2/s. The steady state net flow for $T = 0.21$ s has the direction in the counterclockwise and the Reynolds number is around 89.

The motions of wave along the flexible segment. Although we presented the motions of wave along the flexible segment for the special cases in the previous paper, the fluid mechanism induced by the motions of wave along the flexible segment is so much interesting to present one more time in this paper.

In the previous work, we found that the clockwise net flow seems to be associated with a standing wave in the flexible segment, whereas the counterclockwise net flow seems to be associated with a traveling wave via a peristaltic mechanism. We have observed the same mechanisms for the wave motions along the flexible boundary, although the flows are induced by the new forcing function.

Figure 10 displays the sixteen equal-time snapshots over one cycle of the periodic steady state motions along the top of the flexible segment. The maximum clockwise net flow, almost zero net flow, and maximum counterclockwise net flow is considered at the top, middle, and bottom frame, respectively. Remind that in all three cases, the driving forces are applied on the left 1/3 of the flexible segment, that is the interval from (4 cm, 2.6 cm) to (6.7 cm, 2.6 cm) in the computational rectangular box. In the top frame (maximum clockwise flow), the wave motions along the flexible segment is associated with a standing wave pattern with one node at near the edge of the driven part of the flexible boundary. The number of waves along the flexible segment is just one (long wave), and the amplitude of the physical boundary positions is big enough to produce the active motions of the flexible boundary. Note that the diameter of the tube is 0.6 cm. In the middle frame (almost zero flow), there is also a standing wave pattern with one node at near the edge of the driven part of the flexible boundary. This wave motions along the flexible boundary, especially the driven part of the flexible boundary, remind us our choice of the forcing function that consists of the compression for the half of the period and the relaxation for the rest half of the period because of the choice of the compression duration $d = 0.5$. The motions of the physical boundary track almost the motions of the target positions. If we look at very carefully this figure, then the half of curves are located closely to the initial position of the flexible boundary at $y = 2.6$ cm. In the bottom frame (maximum counterclockwise flow), there is a beautiful traveling wave propagating to the right from the edge of the driven part of the flexible boundary. We have actually observed in the movie that some fluid markers follow the motions of the traveling waves along the flexible boundary with vortices in the counterclockwise direction, which might be observed in the peristaltic mechanism.

From these wave motions along the flexible boundary, we could see the phase differences between the target positions and the physical boundary positions. There are substantial phase differences for the maximum clockwise and counterclockwise net flows, but almost zero phase difference for the case of the almost zero net flow.

Flow mixing. Flow mixing is one of important topics in the devices of MEMS. In this subsection, we show the flow mixing by the valveless pumping.

Figures 11 and 12 displays the positions of the 160 fluid markers inside the flow loop of the maximum clockwise net flow at $T = 0.68$ s. The 40 fluid markers marked with stars, pluses, circles, and triangles are chosen from near the inner boundary to the outer boundary at the initial time $t = 0$. Four equal-time snapshots from $t = 0$ s to $t = 6$ s are plotted in Fiugres 11 and 12. In the bottom frame of Figure 11, the poiseuille flow is observed between the almost rigid segments at $t = 2$ s (only three cycles of the driving force are applied). We can see that the fluid markers are mixed without pathern at $t = 6$ s in the bottom frame of Figure 12. Note that the time $t = 6$ s is very small time compared the simulated time considered for most of other simulations. It is a surprise how fast we could get the flow mixing by the valveless pumping.

Flow which is induced by changing the period *during* an experiment: periods $T = 0.68$ s for the first 20 s, $T = 1.8$ s for the next 20 s, and $T = 0.21$ s for the last 20 s. Figure 13 displays the angles from the center, $(x, y) = (8$ cm, 4 cm$)$, to the current positions of the two arbitrary fluid markers as a function of the time. The three periods, $T = 0.68$ s (maximum clockwise flow) for the first 20 s, $T = 1.8$ s (almost zero flow) for the next 20 s, and $T = 0.21$ s (maximum counterclockwise flow) for the last 20 s, are chosen. All other parameters are fixed during the simulated time $t = 60$ s. The curves are rapidly increased for the first 1/3 of the simulated time, 20 s, with the period $T = 0.68$ s and then stay almost constants during the middle 1/3 of the simulated time, 20 s, with the period $T = 1.8$ s and then smoothly decreased for the last 1/3 of the simulated time with the period $T = 0.21$ s. This shows that the direction of the two fluid markers is changed from clockwise, and then almost zero net flux, and then to counterclockwise. In this figure, we could only observe that the direction around the flow loop is changed by changing the period. When we watch the movie of this special case, not only the direction of a net flow but also the speed of fluid markers and the motions of wave along the flexible boundary are also changed by changing the period *during* an experiment (see []). This case study shows that the result does not depend on the initial condition.

4 Conclusions

We have presented the simulations of flows driven by pumping without valves using a new driving force that consists of the periodic motions of compression and relaxation. The parameter compression duration was introduced to generate the motions of relaxation. In the current standard cardiopulmonary resuscitation (CPR), the optimal compression duration is chosen as 1/2. This fact was the motivation to change the driving forcing function and we could get a more efficient model of valveless pumping with a new driving forcing function.

As we showed in the previous our paper, the two main phenomena of valveless pumping have been also presented in this paper: (1) Existence of a net flow around the loop of tubing despite the lack of valves. (2) The direction and magnitude of the driving oscillation are depend on the parameters from the driving force, such as frequency, amplitude, compression duration, and fraction compressed.

These four parameters from the driving force were chosen for the parameter studies in order to investigate which parameter set provides a more efficient model and to explain the complicated fluid dynamics in valveless pumping. Our main interest is how these parameters affect the direction and magnitude of a net flow around the loop. The frequency is the most crucial factor to determine the direction and magnitude of a net flow around the loop. The critical points of the amplitude and fraction compressed that change the direction of a net flow around the loop are observed. All three parameters, amplitude, compression duration, and fraction compressed, affect on the magnitude of a net flow, too.

The valveless mechanism in a circulatory system is interesting and attractive research because of not only the mysterious fluid dynamics itself but also the various applications in the area of biology, biomedical engineering and engineering, such as a source of circulation in embryo, other valveless biological systems, thoracic pump mechanism in CPR, and MEMS. The main goal of these real world applications is to provide the more net flux around the circulatory system. For this reason, we chose the three special cases, the maximum clockwise, almost zero, and maximum counterclockwise flows in order to study the flow mechanism of valveless pumping in details. One interesting phenomenon among others is that the wave motions along the flexible boundary seems associated with a standing wave pattern in the cases of the maximum clockwise and almost zero net flows and with a traveling wave pattern in the case of the maximum counterclockwise net flow via a peristaltic mechanism. We presented also the result does not depend on the initial condition and showed flow mixing by the valveless pumping that is one of the important topics in MEMS.

Although we have presented the confidential numerical results and found many interesting phenomena of valveless pumping in the two dimension, it is worth to extend our work to the three dimension. The three dimensional study will provide more realistic models and more applicable to the real world applications.

Acknowledgments

This work was supported by the Applied Mathematical Sciences subprogram of the Office of Science Research, U.S. Department of Energy and performed at the Oak Ridge National Laboratory, managed by UT-Battelle, LLC, for the U.S. Department of Energy under contract DE-AC05-00OR22725.

References

[1] K. M. Arthurs, L. C. Moore, C. S. Peskin, and et al., Modeling arteriolar flow and mass transport using the immersed boundary method, J. Comput. Phys., 147 (1998), pp. 402–440.

[2] C. Beattie, A. D. Guerci, T. Hall, A. M. Borkon, W. Baumgartner, R. S. Stuart, J. Peters, H. Halperin, and J. L. Robotham, *Mechanisms of blood flow during pneumatic vest cardiopulmonary resuscitation*, J. Appl. Physiol., 70 (1991), pp. 454–465.

[3] R. P. Beyer, *A computational model of the cochlea using the immersed boundary method*, J. Comput. Phys., 98 (1992), pp. 145–162.

[4] D. C. Bottino, *Modeling Viscoelastic Networks and Cell Deformation in the Context of the Immersed Boundary Method*, J. Comput. Phys., 147 (1998), pp. 86–113.

[5] R. Cortez and M. Minion, *The Blob Projection Method for Immersed Boundary Problems*, J. Comput. Phys., 161 (2000), pp. 428-453.

[6] J. M. Criley, J. T. Niemann, J. P. Rosborough, S. Ung, and J. Suzuki, *The heart is a conduit in CPR*, Crit. Care Med., 9 (1981), pp. 373.

[7] R. Dillon, L. J. Fauci, and D. Gaver III, *A microscale model of bacterial swimming, chemotaxis and substrate transport*, Journal of Theoretical Biology, 177 (1995), pp. 325–340.

[8] R. Dillon, L. J. Fauci, A. L. Fogelson, and D. Gaver III, *Modeling biofilm processes using the immersed boundary method*, J. Comput. Phys., 129 (1) (1996), pp. 57–73.

[9] L. J. Fauci and C. S. Peskin, *A computational model of aquatic animal locomotion*, J. Comput. Phys., 77 (1988), pp. 85–108.

[10] L. J. Fauci, *Peristaltic pumping of solid particles*, Computers and Fluids, 21 (1992), pp. 583–598.

[11] L J. Fauci and A. L. Fogelson, *Truncated Newton methods and the modeling of complex immersed elastic structures*, Communications on Pure and Applied Mathematics, 46 (1993), pp. 787–818.

[12] L J. Fauci and A. McDonald, *Sperm motility in the presence of boundaries*, Bulletin of Mathematical Biology, 57 (5) (1995), pp. 679–699.

[13] A. L. Fogelson, *A mathematical model and numerical method for studying platelet adhesion and aggregation during blood clotting*, J. Comput. Phys., 56 (1984), pp. 111–134.

[14] A. L. Fogelson and C. S. Peskin, *A fast numerical method for solving the three-dimensional Stoke's equations in the presence of suspended particles*, J. Comput. Phys., 79 (1988), pp. 50–69.

[15] J. Guntzig, S. Nolte, P. Schad, and R. Pfankuchen, *Die Lymphdrainage von Cornea, Limbus und Conjunctiva Klin*, MbL Augenheilkunde, 190 (1987), pp. 491–495.

[16] H. R. Halperin, J. E. Tsitlik, R. Beyar, N. Chandra, and A. D. Guerci, *Intrathoracic pressure fluctuations move blood during CPR: comparison of hemodynamic data with predictions from a mathematical model*, Ann. Biomed. Eng., 15 (1987), pp. 385–403.

[17] W. Harvey, *Exercitatio Anatomica de Motu Cordis et Sanguinis in Animalibus*, Frankford, (1987), Caput 14.

[18] E. Jung, *2-D simulations of valvelelss pumping using the Immersed Boundary Method*, Ph.D. Thesis, Courant Institute of Mathematical Sciences in New York University, 1999.

[19] E. Jung and C. S. Peskin, *Two-Dimensional Simulations of Valvelelss Pumping Using the Immersed Boundary Method*, SIAM J. Sci. Comput., 23, 1 (2001), pp. 19–45.

[20] P. J. Kilner, *Formed flow, fluid oscillation and the heart as a morphodynamic pump (abstract)*, European surgical research, 19, suppl 1 (1987), pp. 89–90.

[21] M. C. Lai and C. S. Peskin, *An immersed boundary method with formal second-order accuracy and reduced numerical viscosity*, 160 (2) (2000), pp. 705–719.

[22] R. J. LeVeque and Z. Li, *The immersed interface method for elliptic equations with discontinuous coefficients and singular sources*, SIAM J. Numer. Anal., 31 (1994), pp.1019–1044.

[23] G. Liebau, *Die Bedeutung der Tragheitskrafte fur die Dynamik des Blutkreislaufs*, Zs Kreislaufforschung, 46 (1957), pp. 428–438.

[24] G. Liebau, *Aus welchem bleibt die Blutforderung durch das Herz bei valvularem Versagen erhalten?*, Z. f. Kreislaufforschg., 45 (1956), pp. 481–488.

[25] G. Liebau, *Die Stromungsprinzipien des Herzens*, Zs Kreislaufforschung, 44 (1955), pp. 677–684.

[26] G. Liebau, *Uber ein Ventilloses Pumpprinzip*, Naturwissenschsften, 41 (1954), pp. 327–328.

[27] D. M. McQueen, C. S. Peskin, and E. L. Yellin, *Fluid dynamics of the mitral valve: physiological aspects of a mathematical model*, Am. J. of physiol., 242 (1982), pp. H1095–H1110.

[28] D. M. McQueen and C. S. Peskin, *Shared-memory parallel vector implementation of the immersed boundary method for the computation of blood flow in the beating mammalian heart*, Journal of Supercomputing, 11 (3) (1997), pp. 213–236.

[29] S. Miyazaki, T. Kawai, and M. Araragi, *A piezo-electric pump driven by a flexural progressive wave*, IEEE Transactions, pp. 283–288, 1991.

[30] K. L. Moore, *Embryologie*, Schattauer Stuttgart, 2nd ed (1985), pp. 340–358.

[31] M. Moser, J. W.Huang, G. S. Schwarz, T. Kenner, and A. Noordergraaf, *Impedance defined flow, generalisation of William Harvey's concept of the circulation - 370 years later*, International Journal of Cardiovascular Medicine and Science, Vol 1, Nos 3/4 (1998), pp. 205–211.

[32] C. S. Peskin, *Flow patterns around heart valves: A digital computer method for solving the equations of motion*, Ph.D. Thesis, Albert Einstein College of Medicine, 1972.

[33] C. S. Peskin, *Numerical analysis of blood flow in the heart*, J. Comput. Phys., 25 (1977), pp. 220–252.

[34] C. S. Peskin et al., *Three dimensional fluid dynamics in a two-dimensional amount of central memory. Wave Motion: Theory*, Modeling and Computation, 1 (1987), pp. 85–146.

[35] C. S. Peskin and D. M. McQueen, *A three-dimensional computational method for blood flow in the heart: Immersed elastic fibers in a viscous incompressible fluid*, J. Comput. Phys., 81 (1989), pp. 372–405.

[36] C. S. Peskin and D. M. McQueen, *A general method for the computer simulation of biological systems interacting with fluids*, Symposia of the Society for Experimental Biology, 49 (1995), pp. 265–276.

[37] C. S. Peskin and D. M. McQueen, *Fluid dynamics of the heart and its valves*, Case studies in mathematical modeling - Ecology, Physiology, and Cell Biology, pp. 309–337, 1996.

[38] C. S. Peskin and B. F. Printz, *Improved volume conservation in the computation of flows with immersed elastic boundaries*, J. Comput. Phys., 105 (1993), pp. 33–46.

[39] A. M. Roma, C. S. Peskin, and M. J. Berger, *An adaptive version of the Immersed Boundary Method*, J. Comput. Phys., 153 (1999), pp. 509–534.

[40] M. E. Rosar, *A three dimensional model for fluid flow through a collapsible tube*, PhD thesis, New York University, 1994.

[41] D. J. Randall and P. S. Davie, *The Hearts and Heart-like Organs*, Academic Press, London, 1 (1980), pp. 51–53.

[42] H. Thomann, *A Simple Pumping Mechanism in a Valveless Tube*, Journal of Applied Math. and Phys., 29 (1978), pp. 169–177.

[43] J. A. Werner, M.D., H. L. Greene, M.D., C. L. Janko, and L. A. Cobb, M.D., *Visualization of cardiac valve motion in man during external chest compression using two-dimensional echocardiography.: implications regarding the mechanism of blood flow*, Circulation, 63 (1981), pp. 1417–1421.

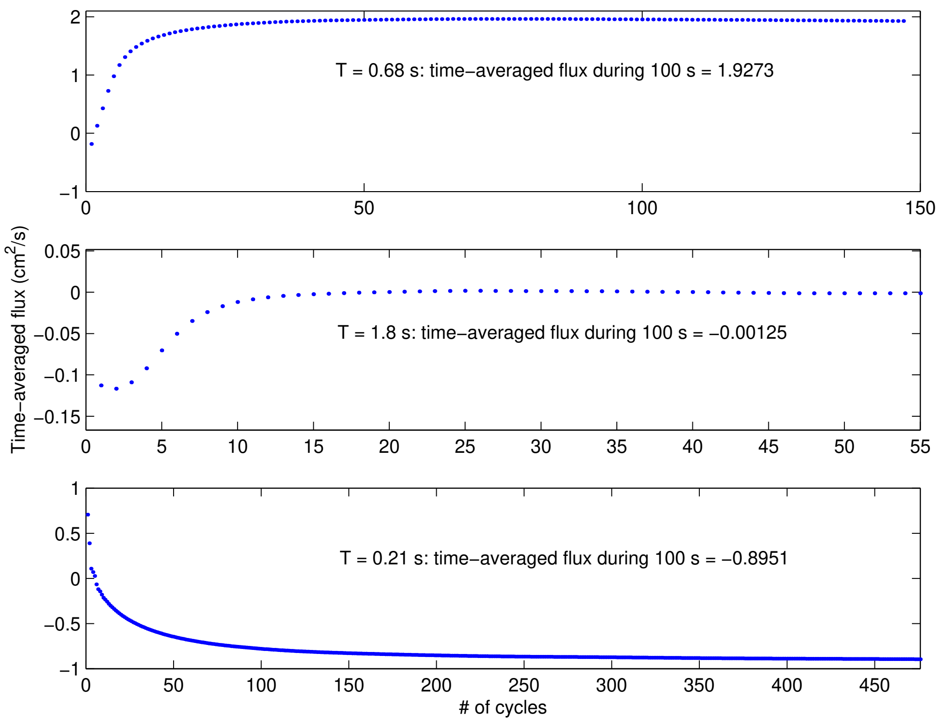

Figure 9: The time-averaged fluxes as functions of the pumping cycles are computed on the vertical cross section through the middle of the straight segment of tubing at the top of the racetrack. The case of maximum average flow in the clockwise direction, almost zero flow, and maximum flow in the counterclockwise direction are considered from top and bottom. Each dot represents the time-averaged flux during the corresponding number of cycle from the beginning $t = 0$.

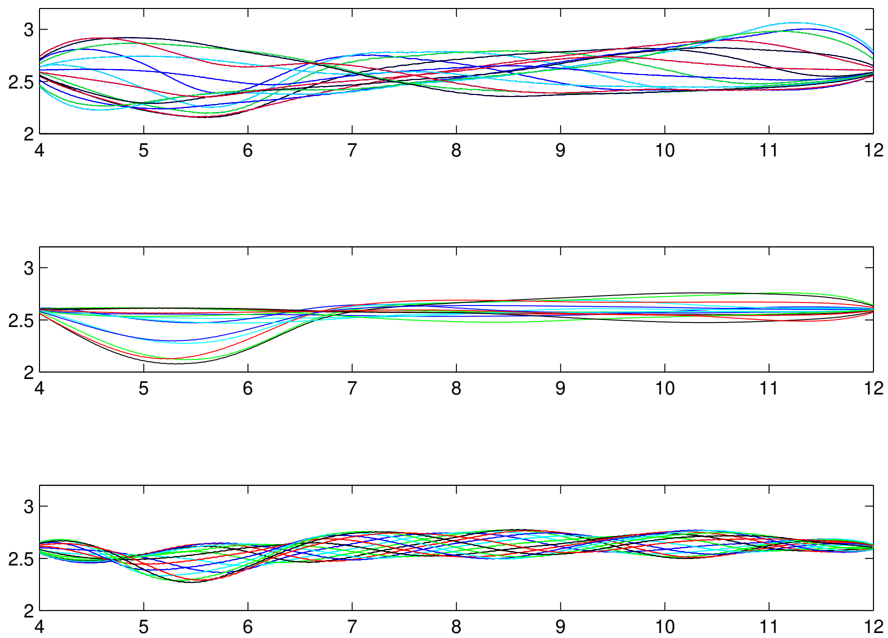

Figure 10: The motions of wave along the flexible segment: Sixteen equal-time snapshots over one cycle of the periodic steady-state wave motions along the top of the flexible segment are plotted. The case of maximum average flow in the clockwise direction, almost zero flow, and maximum flow in the counterclockwise direction are considered from top and bottom. The standing wave patterns are observed for the cases of the maximum clockwise net flow and the almost zero net flow and the traveling wave pattern are observed for the case of the maximum counterclockwise net flow. In all these cases, the driving force is applied on the left 1/3 of the flexible segment, i.e., to the interval from (4 cm, 2.6 cm) to (6.7 cm, 2.6 cm).

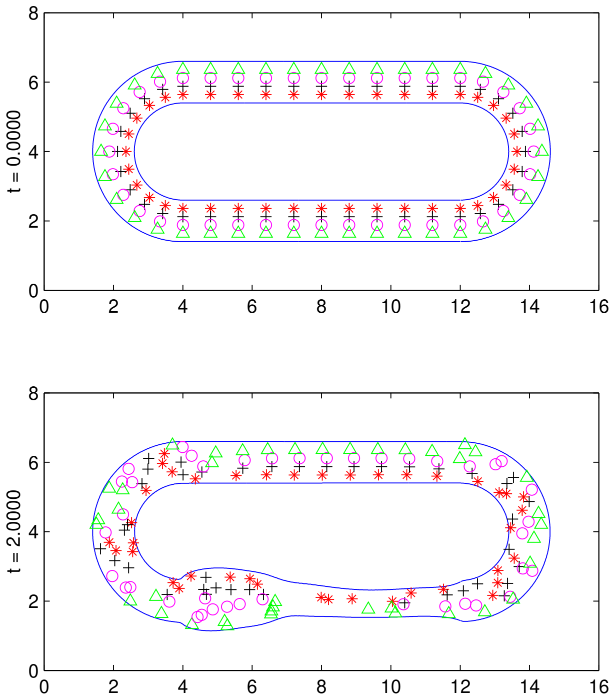

Figure 11: Flow mixing: The positions of the 160 fluid markers inside the flow loop of the maximum clockwise net flow are plotted. Four equal-time snapshots from $t = 0$ s to $t = 6$ s are plotted.

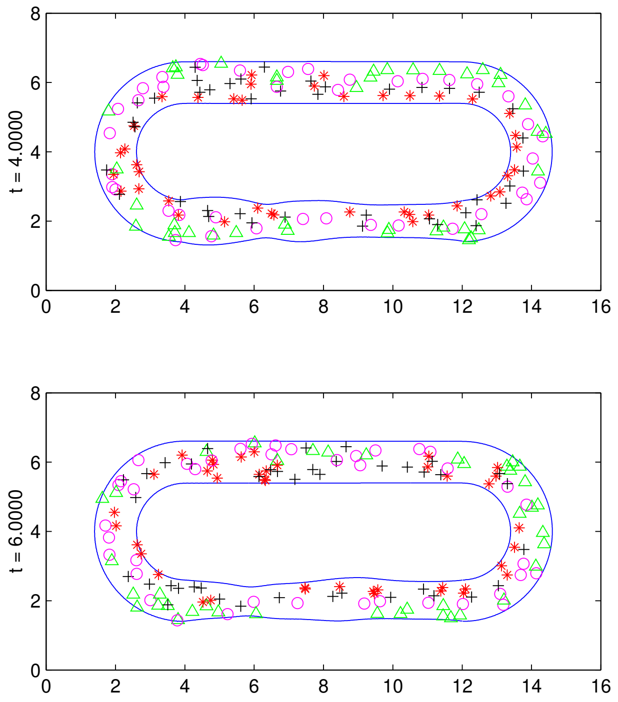

Figure 12: Continuation of Figure 11.

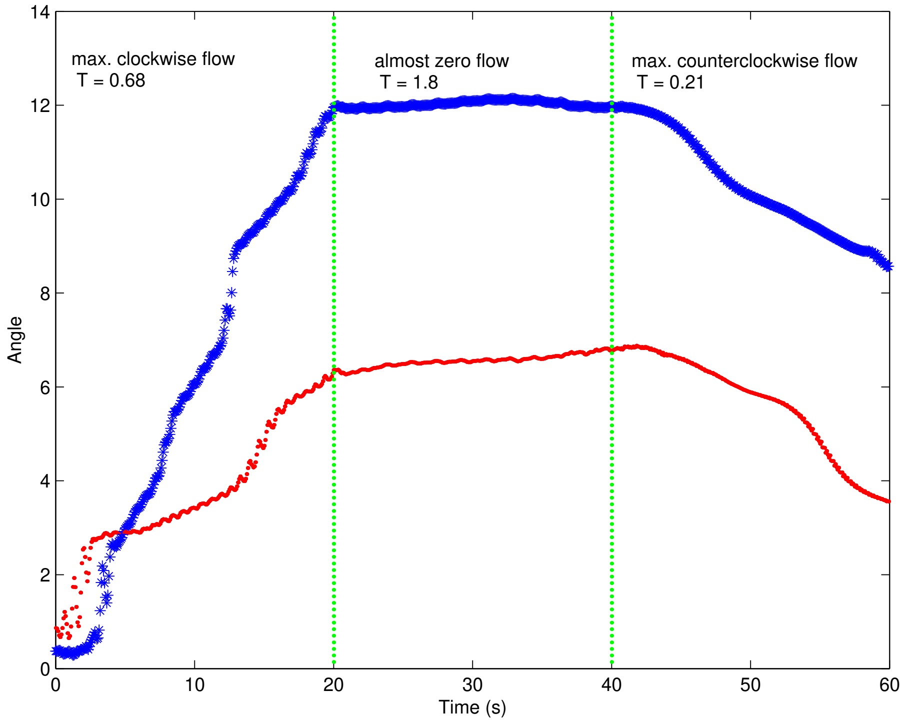

Figure 13: Flow which is changing the direction by changing the period *during* a computer experiment: The angles of the positions of two fluid markers are changed from increasing (clockwise) and stay almost constant (almost zero) and then to decreasing (counterclockwise) in time by changing the period from 0.68 s to 1.8 s at time = 20 s and then from 1.8 s to 0.21 s at time = 40 s. This result shows that the result does not depend on the initial condition.